Broadband Pulse Generation and Radiation with 1.9ps FWHM and 2.5mW Peak Radiated Power based on Direct Digital-to-Impulse Architecture

M. Mahdi Assefzadeh and Aydin Babakhani, Rice University, Houston, TX

Abstract- Broadband signal generation and radiation is demonstrated based on an oscillator-less Direct Digital-to-Impulse (D2I) picosecond pulse radiator with 153GHz 3dB-BW (252GHz 10dB-BW) centered at 140GHz. The radiated pulse achieves a peak EIRP of 15dBm and peak radiated power of 2.5mW. It is shown that the starting time of the radiated pulse is locked to the edge of an input digital trigger with a timing accuracy of better than 270fsec. Frequency-comb spectrum of the radiated pulse train with 5.2GHz repetition rate is characterized up to 1.1THz for a 5.2GHz pulse repetition rate. The measured received SNR at 1.0THz and 1.1THz is 28dB and 22dB, respectively for a distance of 4cm. A 10dB spectral width of 2Hz for the 1.1THz tone is achieved demonstrating extremely high frequency stability (2 part per trillion). Time-domain picosecond pulses are characterized using a fsec-laser-based THz-TDS system. Coherent spatial combining from two widely spaced chips is demonstrated achieving a timing jitter of less than 270fsec. The chip is fabricated in a 130nm SiGe BiCMOS process technology.

Keywords- Integrated circuits, THz, picosecond, direct digital-to-impulse, D2I, on-chip antenna, silicon, SiGe, BiCMOS

I. INTRODUCTION

In the past few years, there has been a growing interest in generation and radiation of ultra-short pulses in the mm-wave and Terahertz (THz) regimes. Picosecond pulse radiation can be used in broadband spectroscopy, 3D imaging, and high-speed wireless communication. In contrast with a bandwidth-limited continuous-wave (CW) radiating source, a picosecond impulse

radiator provides broadband spectral information wide across mm-wave and THz frequencies, which can be used to produce hyper-spectral images. In addition, ultra-short impulses with pulse widths of few picoseconds, and amplitude modulation capability, can be used to build Tbit/sec wireless links.

Traditionally, two different methods are utilized to produce ultra-short pulses in the THz regime. The first method is based on the excitation of a III-V photoconductive antenna (PCA) with a femtosecond laser pulse [1]–[4]. The second method relies on an oscillator followed by a fast switch to turn on/off the pulse [5]–[7]. In this section, we will review these methods and explain their limitations.

A. Picosecond Pulse Radiation based on a PCA Excited by a Femtosecond Laser

In these systems, an optical pulse pump from a femtosecond laser causes terahertz pulse radiation (or detection) by abruptly changing the carrier concentration in a photoconductive switch at the center of a Photo-Conductive Antenna (PCA). In this case, in the emission mode in which a terahertz impulse is radiated, a DC bias is applied to a PCA. When a femtosecond optical pulse arrives, the photoconductive switch shorts the PCA antenna and generates a fast current with a picosecond rise time. This current drives the antenna and produces THz waves. A similar principle is used to detect the THz pulses. In this case, no DC bias is applied on the PCA. Instead, a femtosecond laser shorts the junction of the PCA antenna and generates a DC current proportional to the THz signal received by the antenna. To capture the entire waveform, a sub-sampling scheme is utilized, where the measurement is repeated by delaying the laser pulse and shifting the sampling time. This method of THz pulse generation and detection is widely used in THz Time-Domain Spectroscopy (THz-TDS).

THz-TDS has numerous applications in spectroscopy and imaging. In medical imaging, it has been used for skin cancer detection based on the dielectric contrast between the normal and cancerous cells [8], [9]. In addition, it has been used in pharmaceutical applications, nondestructive evaluation of materials [10]–[12], explosive detection, and security imaging [13]–[15].

Although THz-TDS is a powerful technique, it suffers from many limitations. First, it requires a femtosecond laser, which is not only bulky and expensive but has a low repetition rate (<100MHz), which limits the average radiated power. Second, to produce an image, the object has to be mechanically scanned, which significantly reduces the acquisition time. Finally, to capture the entire waveform, a sub-sampling scheme is utilized, where a mechanical delay line is used to shift the laser pulse. This mechanical delay-line significantly reduces the measurement speed. These limitations make THz-TDS systems poorly accessible.

B. Oscillator and Switch Based Pulse Radiation

Current silicon-based pulse radiating systems are based on on-chip oscillators followed by a fast switch. These solutions suffer from the random phase variation of the free-running carrier signal or need a complicated area/power-consuming Phase-Locked Loop (PLL) [6]. These solutions suffer from several limitations. First, the bandwidth of the generated pulse is limited by the transient time of the switch or the turn-off time of the VCO. Second, the RF leakage caused by low isolation of a switch at THz frequencies dramatically degrades the performance and dynamic range of the system in radar applications. Third, the VCO and the PLL have to run continuously, which dramatically degrades the power efficiency of the transmitter. Finally, area-consuming PLLs and Delay-Locked Loops (DLL) limit the scalability of these transmitters.

In this work, a novel oscillator-less architecture is proposed and successfully implemented in silicon that overcomes the aforementioned limitations.

II. Direct Digital-to-Impulse Radiation

In this section, the architecture of a Direct Digital-to-Impulse (D2I) is reported that converts a low-frequency digital trigger to a radiated THz pulse. In this architecture, the starting time of the radiated pulse is synchronized with the edge of the input trigger with a high timing accuracy [16], [17]. In addition, the pulse-width of the radiation is minimized using an impulse-shaping network. In the D2I architecture, a magnetic energy is accumulated by flowing DC current through a broadband, phase-linear antenna, which acts as an inductor in low frequencies. This antenna is placed in series with a fast current switch. By opening the switch, the DC current on the antenna is interrupted, which results in converting the stored magnetic energy to a radiated impulse in the THz regime. In addition, an intermediate impulse-shaping network is designed to maximize the amplitude of the pulse and minimize ringing.

A. Fundamentals of D2I

The D2I method of on-chip impulse radiation is inspired by numerous physical phenomena with similar mechanisms. For example, the first wireless telegraphy technique was built with spark gap transmitters. This transmitter radiated pulsed electromagnetic waves generated by a fast flow of current through the spark gap and a voltage pulse induced on an antenna [18].

The magnetic energy stored in an antenna structure having a circulating DC current of i_0 is expressed as,

$$E_{DC} = \iiint_{-\infty}^{\infty} \frac{1}{2\mu(x,y,z)} B_0^2(x,y,z)\, dx\, dy\, dz = \frac{1}{2}\Phi_0 i_0 = \frac{1}{2} L_0 i_0^2, \tag{1}$$

where $\mu(x,y,z)$ is the permeability in space, $B_0(x,y,z)$ is the stored DC magnetic flux density, Φ_0 is the stored magnetic flux, and L_0 is the inductance of the antenna at DC. The real part of the antenna impedance at DC is negligible and only plays a dissipative role without changing the stored DC energy. The stored energy can also be written in terms of the reactive part of the antenna impedance, X_{ant}:

$$E_{DC} = \frac{1}{2} L_0 i_0^2 = \left. \frac{X_{ant} i_0^2}{2\omega} \right|_{\omega \to 0}. \tag{2}$$

From (1), it can be understood that circulating a larger DC current and having a higher inductance for the antenna stores a higher magnetic energy. In this work, for a 100mA current, the stored magnetic energy is 540fJ (L = 108pH).

The process of releasing the stored magnetic energy into a radiated impulse is done by switching a broadband phase-linear antenna, through an intermediate impulse-shaping network. The impulse-shaping network is utilized to minimize the ringing while maximizing the peak amplitude of the radiated pulse. Fig. 1 shows a system-level block diagram of this mechanism. In section III, these systems are individually modeled and analyzed.

B. Bandwidth, Jitter, Efficiency, and Scalability of D2I

In D2I, the deep nonlinear switching mechanism results in numerous harmonics from GHz to THz. Having a high-power, broadband frequency-comb source is critical in imaging and spectroscopy applications. By applying a periodic trigger signal, the D2I architecture radiates an impulse train in the time domain with the same repetition rate as the input trigger signal. Considering $x(t)$ as the time-domain signal of a single impulse, the time-domain impulse train can be written as,

$$y(t) = x(t) * \sum_{k=-\infty}^{\infty} \delta(t - kT) = \sum_{k=-\infty}^{\infty} x(t - kT), \tag{3}$$

where T is the period of the impulse train. By taking the Fourier transform of $y(t)$ we will have,

$$Y(f) = \frac{1}{T} X(f) \sum_{k=-\infty}^{\infty} \delta\left(f - k\frac{1}{T}\right), \tag{4}$$

in which $X(f)$ is the Fourier transform of a single impulse signal. Thus, the frequency spectrum of an impulse train is a sampled version of the frequency spectrum of a single impulse with steps of $1/T$. To perform spectroscopy, T can be controlled to sweep the whole spectrum.

In D2I topology, the starting time of the impulse radiation is locked to the edge of the input trigger with a stable repetition rate. This results in ultra-stable generation of frequency tones, *e.g.* 2Hz at 1.1THz is achieved in this work. In addition, by eliminating the on-chip high-frequency VCO and its required PLL, the conversion efficiency from the DC energy to THz increases and the area of the chip becomes smaller. It is important to note that, to minimize the power consumption, the current switch can be turned on shortly before the edge of the trigger arrives and does not have to be kept on.

C. Broadband High-Directivity Beamsteering with D2I

Conventionally, different methods for beamsteering are utilized in phased-array architectures. These methods are suitable for narrowband phased arrays. In the first method, the time delay is introduced in the signal path by using tunable transmission-lines based on non-linear varactors [19]. The main disadvantage of the signal-path delay elements are their nonlinearity and signal-dependent behavior. This is because the waveform of the information signal varies with time, which results in an undesired waveform-dependent delay. In the second method, delay generation is performed by phase shifting the LO signal at the LO-path [20]–[22]. This method is inherently

narrowband and only works at a single frequency. In the third method, the time delay is generated in baseband using a digital processor [23]. In this method, a large number of complex digital processors are needed that increase the complexity of the system.

In the D2I architecture, the information signal is stored at the location of the radiator. By delaying the trigger signal, the radiated pulse is delayed. Since the delay path is separated from the signal path (information path), the information content of the signal does not affect the generated delay. In addition, since the time-domain waveform of the trigger signal is always constant and does depend on the information signal (Fig. 2), nonlinearity of the delay generator does not degrade the performance of the system. This method enables broadband delay of the radiated signal with accuracy of close to 150fsec [17], which is limited by the timing jitter of the system. Unlike LO-phase shifting schemes [20]–[22], due to the broadband nature of the delay mechanism in D2I, it is possible to build a high-directive radiating array, where all the frequency contents of the signal are precisely steered together.

III. On-chip Antenna and Circuit Details

A. On-Chip Impulse Antenna

In order to attain a large bandwidth, high efficiency, and low cost, the D2I design needs to be implemented using on-chip antennas. An on-chip antenna provides a large bandwidth by removing the lossy and narrowband connections (e.g. wire-bond) between the chip and an off-chip antenna. It also reduces the cost of assembly by eliminating the need for precise alignment of the off-chip antenna. In this work, a slot bow-tie on-chip antenna is designed and successfully tested. In addition, the antenna impedance as well as its near and far field responses are carefully simulated.

One of the important challenges in designing an efficient broadband on-chip antenna is the substrate modes. Substrate modes make the antenna narrow-band, reduce its efficiency, and cause undesired ringing. They also introduce substantial nonlinearity in the phase response of the antenna. In order to avoid these undesired effects of the planar substrate, a hemispherical high resistivity silicon lens is attached under the chip to mimic a semi-infinite silicon substrate for the antenna. The silicon lens increases the radiation efficiency by minimizing the loss of substrate modes and maximizes the bandwidth by avoiding substrate reflections.

To minimize the pulse-width of the radiated impulse, the antenna needs to have a broadband impulse response with a linear phase. In addition, the D2I topology requires an antenna that behaves like an inductor in low frequencies. To address these requirements, a slot bow-tie antenna is designed and optimized by adjusting its dimensions and curving its edges to enhance the bandwidth. Fig. 3 shows the geometry of the slot bow-tie antenna, which is fabricated using an on-chip copper metal layer (M5) with a thickness of 1.5 μm. The antenna radiates to the substrate of the silicon chip, which is mounted on the back of a high-resistivity silicon lens. The thickness of the silicon substrate is 200μm and its resistivity is 10Ω.cm. The silicon lens is a hemispherical lens with an extension length of 300μm and a resistivity of 10,000Ω.cm.

Two shielded microstrip transmission lines are used as a differential pair to feed the antenna. Near-field of the antenna is simulated to locate a suitable spot for the feed structure. Electric field in x and y directions at 12μm above the antenna plane is plotted in Fig. 3. As shown in this figure, to minimize the effect of the transmission lines on the antenna current, they are placed along the x-direction at the center of the antenna, where $E_x = 0$. The width of the horizontal feeds is minimized to reduce the effect on the E_y. In addition, circuit components are placed distant from the sharp corners of the antenna, where E-field is large. Fig. 4 shows the input impedance and

radiation efficiency of the slot bow-tie antenna. The small ringing effects in impedance and radiation efficiency are caused by the internal reflections inside the silicon lens.

B. Near- and Far-Field Responses

The slot bow-tie antenna can be modeled as a single-input double-output system, where its input is the antenna current. One of the outputs of the antenna is the voltage induced on the antenna. The other output is the radiated electric field in a far-field location. The induced voltage on the antenna is affected by the near-field of the antenna, which has a different response than the far-field. The near field response directly affects the switching performance of the active core circuit and the nearby radiating elements in case of an array. Since the ultimate goal is to radiate short pulses in the far-field, the design is optimized to minimize pulse-width of the radiated signal in the far-field.

Assuming a semi-infinite silicon substrate under the chip, the voltage and far-field E-field responses of the antenna are simulated and shown in Figs. 5-6. The near- and far-field impulse responses of this system are modeled with different LTI transfer functions, with orders of 2 and 4, respectively. The simulated near- and far-fields time-domain responses are shown in Fig. 5 and their frequency spectrum and group delays are shown in Fig. 6. In addition, we have extracted the zeros and poles of these two transfer functions and plotted the results in Fig. 7. By comparing the magnitude and group delay of the transfer functions, it is observed that the far field response has a much larger bandwidth. In addition, the strong ringing effects on the antenna voltage is mostly due to non-radiative near-field.

The far-field radiation pattern of the impulse antenna is calculated by using the actual silicon lens, instead of a semi-infinite silicon, in an FDTD electromagnetic simulator (CST). Fig. 8 plots the E- and H-plane far-field patterns at $f_0 = 140\text{GHz}$, which is the center frequency of the

radiated pulse measured in section IV. In addition, a comparison between the simulated E-plane patterns at f_0, $f_{-3dB,1} = 67\text{GHz}$, and $f_{-3dB,2} = 220\text{GHz}$ are shown in Fig. 9.

C. D2I Circuit Schematic

The circuit schematic of the THz impulse radiator is shown in Fig. 10. A low-power digital trigger with a rise time of 150ps is fed to the input of the chip. A set of inverter stages buffer the input trigger and sharpen its rise time to 30ps. Following the digital buffers, an edge-sharpening amplifier is designed that employs inductive peaking to further sharpen the rise time to less than 10ps. This signal is then coupled to a current switch implemented by a cascode pair of bipolar transistors. An array of distributed capacitors is used to couple the output of the edge-sharpening amplifier to the current switch. Capacitor arrays are also used at the biasing nodes to provide a broadband low-impedance termination. The performance of the current-switch is observed using two parameters: the switching speed and the rate of change in the current. These parameters determine the pulse-width and peak power of the radiated THz impulse. The current switch is biased at a deeply nonlinear region and generates pulses with Full Width at Half Maximum (FWHM) of less than 2ps. The effects of the biasing and supply voltage of the current switch on the radiated pulse are studied in section IV.

In the D2I architecture, a cascode current-switch is favored over a single bipolar switch because of the following reasons: First, the cascode switch minimizes the loading effect on the previous stage by avoiding the Miller effect. Second, the output resistance of the casocde switch is much larger than a single transistor, which increases the amplitude of the radiated impulse.

In this design, an array of transmission line and capacitors are used to provide fast charge delivery at the time of switching and minimize the effect of the bond wire. Instead of using a single bypass capacitor from the bondpad to ground, a series of smaller capacitors with much

higher resonance frequency are embedded in a transmission line to provide a near-ideal supply voltage to the circuit and absorb rapid changes in the current of the antenna.

The characteristic impedance of the transmission lines and the unit capacitance of the capacitor arrays are optimized to maximize the amplitude of the E-field in the far-field and minimize the pulse width. Transient simulations are performed to find these optimum parameters for the current-switch stage. The LTI models for antenna's impedance and far-field response are used to create a two port model of the antenna, as shown in Fig. 11. The simulated far-field E-field is shown in Fig. 12.

IV. Chip Characterization in both Time and Frequency Domains

A. Time-Domain Characterization with a Femtosecond-Laser-based THz-TDS System

One of the main challenges in sampling a picosecond pulse in the time domain is the receiver and its antenna. The receiver and the antenna need to be broadband and have a linear phase response. Pyramidal horn antennas cannot be used to receive picosecond pulses due to their limited bandwidth and nonlinear phase response [24]. In addition, available commercial sampling oscilloscopes have a 3-dB bandwidth of less than 110GHz. They cannot be used to sample a pulse with FWHM of ~2psec.

In this work, a novel time-domain measurement system is developed to characterize the time-domain waveform of the radiated pulses using a THz-TDS system equipped with a photoconductive antenna (PCA). An Advantest TAS7500TS fsec-laser-based THz sampling system is used to capture the time-domain signal radiated from the chip. On the receiver side, an Advantest TAS1230 PCA samples the THz waveform. The laser repetition rate is 50MHz. The repetition frequency of the impulse radiating chip is synchronized with the laser using a custom

synchronization chain, as shown in Fig. 13. This setup synchronizes a Keysight E8257D signal generator with a 50MHz electrical signal extracted from the pulsed-laser. The 50MHz electrical signal is conditioned and its frequency is divided by a factor of five. The resulting 10MHz reference signal is fed to the 10MHz reference input of the signal generator.

Fig. 14 shows the measured time-domain waveform of the radiated impulses, which achieve a FWHM of 1.9ps and a minimum-to-maximum time of 2.7ps. The FFT of the time-domain signal is shown in Fig. 16. This measured frequency spectrum has a center frequency of 140GHz and a 3-dB bandwidth of 153GHz, which translates to a 3-dB fractional bandwidth of 111%. The time-domain E-plane radiation pattern of the impulse radiator is measured in terms of pulse peak power and pulse width. These results are shown in Fig. 16. Based on this characterization, the FWHM of the radiated impulse changes from 1.9ps at 0° elevation angle to 2.8ps at the elevation angle of 60°. The FWHM of the pulse is 2.2ps at 30°.

The current-switch stage in this design is based on a cascode architecture. Changes in the bias voltages of the current-switch stage affect the amplitude of the radiated pulse. The effects of input biasing of this stage, V_3, and the supply voltage, V_{CC}, are experimented in Fig. 17. In this figure, a 3D surface graph plots the normalized peak power of the radiated pulse versus input biasing and supply voltage of the current-switch. These two voltages affect the amplitude of the radiated pulse by varying the nonlinear parasitic capacitances of the transistor and its current. As shown in Fig. 17, the maximum peak power of the radiated pulse does not necessarily occur at the highest supply voltage.

The peak pulse EIRP and peak radiated power of the THz impulse radiator are calculated based on the time-domain measurements. In the EIRP measurement, no Teflon lens is used and the receiver is placed at a distance of 2cm from the chip. The peak voltage of the received pulse

in this measurement is 12mV. In order to calculate the EIRP based on the Friis formula, the gain of the receiver must be calibrated. This calibration is performed using frequency-domain measurement at 140GHz (center frequency of the pulse spectrum). Based on this measurement, the calibrated gain of the receiver at 140GHz is $G_r = 1\text{dB}$. Also, the received peak power based on the time-domain measurements is $P_r = -25dBm$. Thus, the peak EIRP of the radiator, calculated based on the receiver gain of 1dB at the center frequency of the pulse (140GHz), distance of R=2cm, is

$$EIRP_{peak} = \frac{P_r}{G_r}\left(\frac{4\pi R}{\lambda}\right)^2 = 15\text{dBm} \tag{5}$$

where $\lambda = 2.1mm$ is the wavelength at the center frequency of 140GHz. Based on the measured peak pulse EIRP and the simulated transmitter gain at 140GHz ($G_t = 11\text{dB}$), the peak radiated power is also calculated as $P_t = \frac{EIRP_{peak}}{G_t} = 2.5\text{mW}$.

B. 0.05-1.1THz Frequency-Domain Measurements

The performance of the chip is independently characterized using a frequency-domain measurement setup, as shown in Fig. 18. The mixer port of a Keysight N9030A PXA Signal Analyzer is used with OML Harmonic Mixers and Horn Antennas WR-15, 10, 08, 05, 03 to cover 0.05-0.325THz and with VDI SAX and Horn Antennas WR-2.2, 1.5, 1.0 to cover 0.33-1.1THz. The distance between the chip and the horn antenna is greater than 4cm in all of the measurements. A 5.2GHz trigger signal with 10dBm power is fed to the 50Ω input of the chip through a bias-T. The generated frequency tones of the radiated are measured at the harmonics of 5.2GHz, from 50GHz to 1.1THz.

Fig. 19 shows the measured frequency stability and the received SNR after down conversion. The SNR is limited by the path loss and noise figure of the down-conversion mixer. This figure

shows the frequency tones measured at 1.10THz, 1.08THz, 0.9THz, 0.81THz, 0.75THz, and 0.6THz. The measured received SNR in these frequencies are 20dB, 33dB, 40dB, and 40dB, respectively. The SNR numbers reported are measured at the receiver, which is at a distance of at least 4cm from the chip, hence the SNR at the transmitter is much higher. The average Effective Isotropic Radiated Power (EIRP) of the radiator is calculated based on the frequency domain measurements for the entire 0.05-1.1THz frequency range and plotted in Fig. 21. The EIRP numbers are calculated based on the Friis formula. It should be noted that the numbers reported in Fig. 20 are average EIRP values for the pulse radiator with 1.9ps FWHM and a pulse-to-pulse spacing of 192ps (5.2GHz repetition rate). The fluctuation in the plot in Fig. 20 is due to using several different mixers and antennas, and reflections from surrounding objects. This effect emphasizes the accuracy of coherent time-domain THz-TDS characterization introduced in section IV.A. is The peak EIRP and peak radiated power are calculated based on the time-domain measurement and reported in subsection IV.C. The frequency-domain radiation pattern of the THz impulse radiator chip is also measured at two frequency components: the center frequency of 140GHz and the maximum frequency of 1.1THz. Figs. 21-22 plot the E- and H-plane radiation patterns at these frequencies. The measured directivities at 140GHz and 1.1THz, are 16dBi and 18dBi, respectively. The pattern at 1THz has more lobes as expected.

V. Coherent Spatial Combining of Impulses From Widely Spaced Radiators

Precision synchronization between the digital trigger and the radiated impulse enables coherent combining of radiated impulses from widely spaced antennas with increased effective aperture size. To demonstrate this, the radiated THz pulses from two separate widely spaced chips are combined in space. The measurement setup of this experiment is shown in Fig. 23. Due to the difficulties in the measurement of two radiators with the THz-TDS system, a custom PCB-

based inverted cone planar antenna is designed and used as the receiving antenna in this experiment. The receiving antenna is directly connected to a Keysight remote sampling head 86118A. Fig. 23 shows that the measured combined signal matches with the algebraic some of the received signals radiated from individual chips. The timing jitter of the combined signal is calculated by a Keysight 86100DCA sampling oscilloscope, which resulted in an RMS jitter of 270fs for an averaging of 64 (Fig. 24). The measured jitter for averaging of 256 and 512 is 220fs and 130fs, respectively.

The chip is fabricated in 130nm SiGe BiCMOS process with an f_T of 200GHz and an f_{max} of 280GHz. Table I compares the performance of the chip with the prior work. Finally, a micrograph of the chip is shown Fig. 25, which occupies an area of 550μm × 850μm and consumes 220mW DC power.

VI. Conclusion

A fully-integrated impulse radiator chip based on a novel oscillator-less direct digital-to-impulse architecture is introduced that is capable of radiating THz pulses with FWHM of 1.9ps and 3dB-BW of 153GHz (10dB-BW of 252GHz) centered at 140GHz. The starting time of the radiated impulses is locked to the edge of the input digital trigger. The chip fed by a stable trigger signal radiates harmonic tones up to 1.1THz (limited by receiver) with an ultra-high spectral purity. Broadband 0.05-1.1THz signal generation and radiation is demonstrated with a received SNR of 22dB at 1.1THz, 28dB at 1.0THz, and 30dB at 0.9THz. A 10dB-below-peak spectral width of only 2Hz at 1.1THz is measured that shows extremely high frequency stability. A novel time-domain THz pulse sampling system is developed using a femtosecond-laser-based THz-TDS system. The effect of the bias and supply voltages of the current switch stage on the radiated impulses is studied based on the measurement.

REFERENCES

[1] S. Matsuura, M. Tani, and K. Sakai, "Generation of coherent terahertz radiation by photomixing in dipole photoconductive antennas," *Appl. Phys. Lett.*, vol. 70, no. 5, p. 559, 1997.

[2] N. Chimot, J. Mangeney, L. Joulaud, P. Crozat, H. Bernas, K. Blary, and J. F. Lampin, "Terahertz radiation from heavy-ion-irradiated In0.53 Ga 0.47As photoconductive antenna excited at 1.55 ??m," *Appl. Phys. Lett.*, vol. 87, no. 19, pp. 1–3, 2005.

[3] N. M. Froberg, B. Bin Hu, X. C. Zhang, and D. H. Auston, "Terahertz Radiation From a Photoconducting Antenna Array," *IEEE J. Quantum Electron.*, vol. 28, no. 10, pp. 2291–2301, 1992.

[4] B. Salem, D. Morris, V. Aimez, J. Beerens, J. Beauvais, and D. Houde, "Pulsed photoconductive antenna terahertz sources made on ion-implanted GaAs substrates," *J. Phys. Condens. Matter*, vol. 17, no. 46, pp. 7327–7333, 2005.

[5] A. Arbabian, S. Callender, S. Kang, M. Rangwala, and A. M. Niknejad, "A 94 GHz mm-Wave-to-Baseband Pulsed-Radar Transceiver with Applications in Imaging and Gesture Recognition," *Solid-State Circuits, IEEE J.*, vol. 48, no. 4, pp. 1055–1071, Apr. 2013.

[6] X. Wu and K. Sengupta, "Dynamic Waveform Shaping for Reconfigurable Radiated Periodic Signal Generation with Picosecond Time-width," 2015.

[7] P. Chen and A. Babakhani, "A 30GHz impulse radiator with on-chip antennas for high-resolution 3D imaging," *2015 IEEE Radio Wirel. Symp.*, pp. 32–34, 2015.

[8] R. M. Woodward, V. P. Wallace, D. D. Arnone, E. H. Linfield, and M. Pepper, "Terahertz Pulsed Imaging of Skin Cancer in the Time and Frequency Domain," *J. Biol. Phys.*, vol. 29, no. 2, pp. 257–259.

[9] E. Pickwell, B. E. Cole, a J. Fitzgerald, M. Pepper, and V. P. Wallace, "In vivo study of human skin using pulsed terahertz radiation.," *Phys. Med. Biol.*, vol. 49, no. 9, pp. 1595–1607, 2004.

[10] C. J. Strachan, P. F. Taday, D. A. Newnham, K. C. Gordon, J. A. Zeitler, M. Pepper, and T. Rades, "Using terahertz pulsed spectroscopy to quantify pharmaceutical polymorphism and crystallinity," *J. Pharm. Sci.*, vol. 94, no. 4, pp. 837–846, 2005.

[11] C. D. Stoik, M. J. Bohn, and J. L. Blackshire, "Nondestructive evaluation of aircraft composites using transmissive terahertz time domain spectroscopy," *Opt. Express*, vol. 16, no. 21, pp. 17039–17051, Oct. 2008.

[12] Y. C. Shen and P. F. Taday, "Development and application of terahertz pulsed imaging for nondestructive inspection of pharmaceutical tablet," *IEEE J. Sel. Top. Quantum Electron.*, vol. 14, no. 2, pp. 407–415, 2008.

[13] C. Baker, T. Lo, W. R. Tribe, B. E. Cole, M. R. Hogbin, and M. C. Kemp, "Detection of concealed explosives at a distance using terahertz technology," *Proc. IEEE*, vol. 95, no. 8, pp. 1559–1565, 2007.

[14] H.-B. Liu, H. Zhong, N. Karpowicz, Y. Chen, and X.-C. Zhang, "Terahertz Spectroscopy and Imaging for Defense and Security Applications," *Proc. IEEE IEEE*, vol. 95, no. 8, pp. 1514–1527, 2007.

[15] J. Chen, Y. Chen, H. Zhao, G. J. Bastiaans, and X.-C. Zhang, "Absorption coefficients of selected explosives and related compounds in the range of 0.1-2.8 THz.," *Opt. Express*, vol. 15, no. 19, pp. 12060–12067, 2007.

[16] M. Assefzadeh and A. Babakhani, "An 8-psec 13dBm peak EIRP digital-to-impulse radiator with an on-chip slot bow-tie antenna in silicon," in *Microwave Symposium (IMS), 2014 IEEE MTT-S International*, 2014, pp. 1–4.

[17] M. M. Assefzadeh and A. Babakhani, "A 9-psec differential lens-less digital-to-impulse radiator with a programmable delay line in silicon," in *Digest of Papers - IEEE Radio Frequency Integrated Circuits Symposium*, 2014, pp. 307–310.

[18] G. Marconi, "Wireless telegraphy," *Electrical Engineers, Journal of the Institution of*, vol. 28, no. 139. pp. 273–290, 1899.

[19] D. PARKER and D. C. ZIMMERMANN, "Phased arrays-Part II: Implementations, applications, and future trends," *IEEE Trans. Microw. Theory Tech.*, vol. 50, no. 3, pp. 688–698.

[20] H. Hashemi, X. Guan, A. Komijani, and A. Hajimiri, "A 24-GHz SiGe phased-array receiver - LO phase-shifting approach," *IEEE Trans. Microw. Theory Tech.*, vol. 53, no. 2, pp. 614–625, 2005.

[21] A. Natarajan, A. Komijani, X. Guan, A. Babakhani, and A. Hajimiri, "A 77-GHz Phased-Array Transceiver With On-Chip Antennas in Silicon: Transmitter and Local LO-Path Phase Shifting," *Solid-State Circuits, IEEE J.*, vol. 41, no. 12, pp. 2807–2819, Dec. 2006.

[22] A. Babakhani, X. Guan, A. Komijani, A. Natarajan, and A. Hajimiri, "A 77-GHz Phased-Array Transceiver With On-Chip Antennas in Silicon: Receiver and Antennas," *Solid-State Circuits, IEEE J.*, vol. 41, no. 12, pp. 2795–2806, Dec. 2006.

[23] T. S. Rappaport, *Wireless communications: principles and practice*, vol. 2. Prentice Hall PTR New Jersey, 1996.

[24] C. A. Grosvenor, R. T. Johnk, D. R. Novotny, S. Canales, B. Davis, and J. Veneman, *TEM Horn Antenna Design Principles*. 2007.

TABLE OF FIGURES

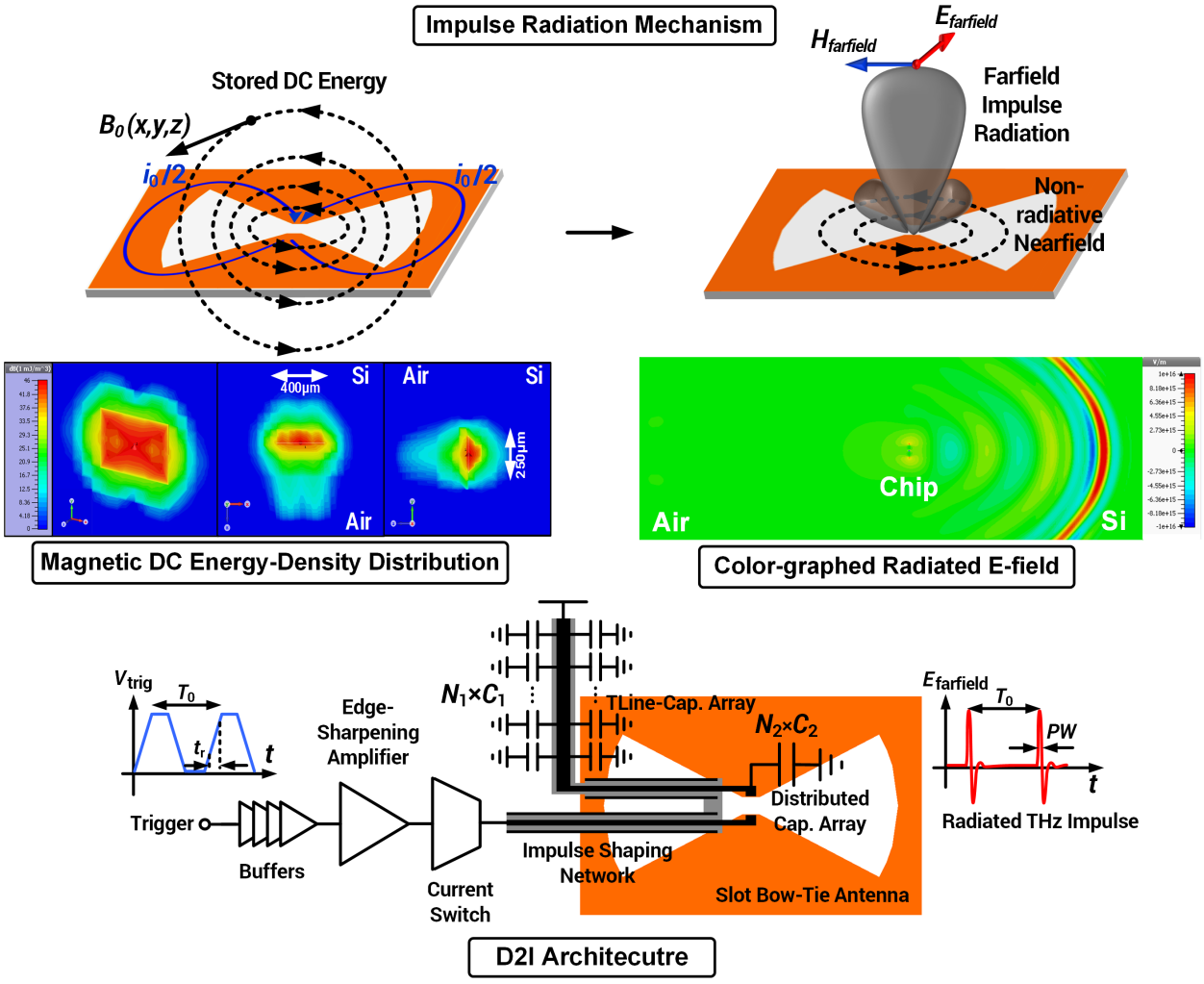

Fig. 1. Physical mechanism of impulse generation and radiation, and architecture of D2I

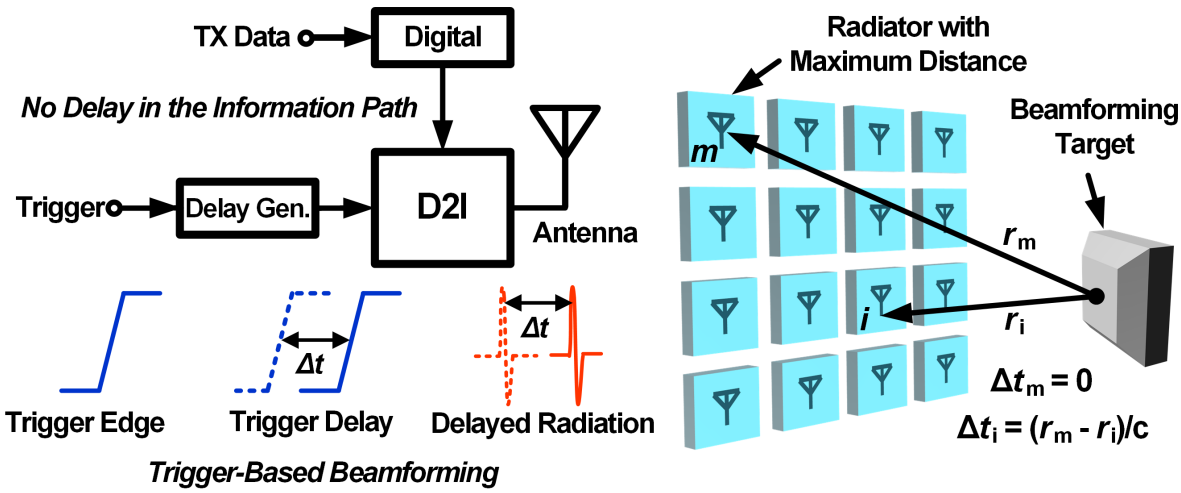

Fig. 2. Trigger-based beamforming architecture

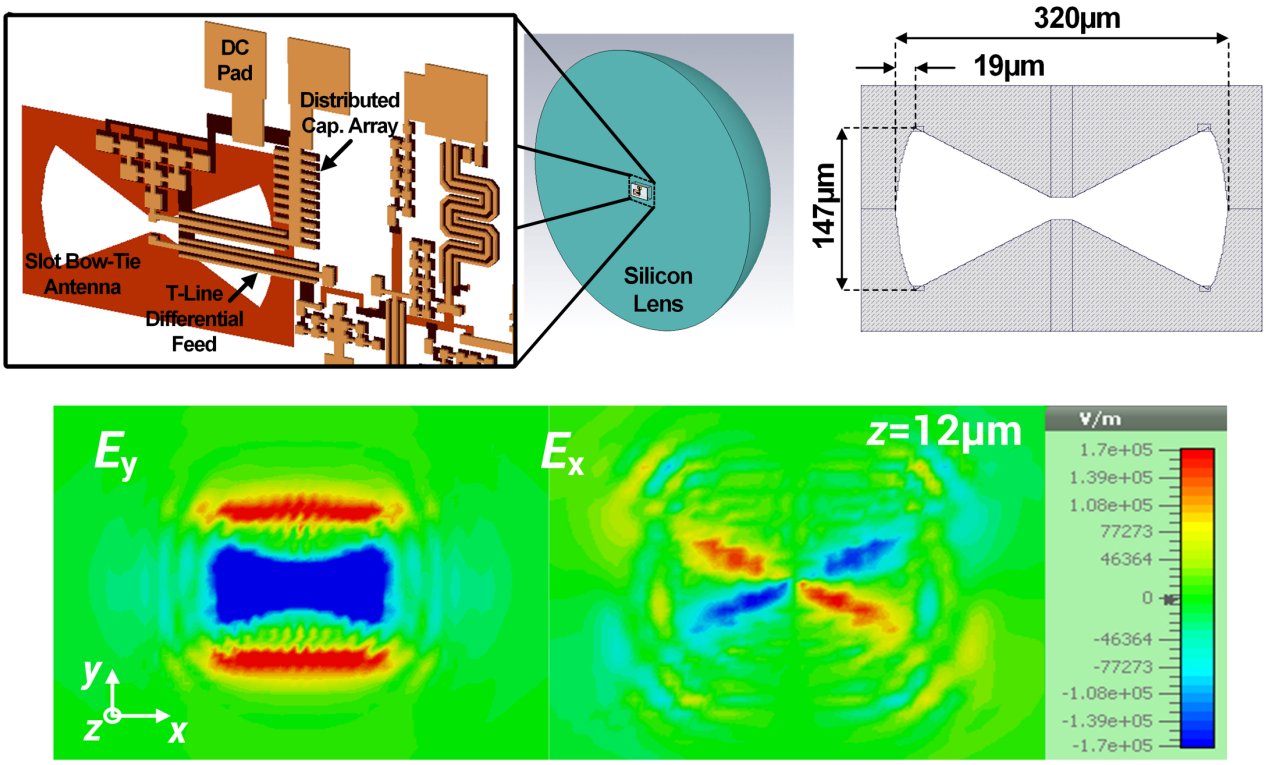

Fig. 3. Antenna geometry and simulated near-field E-field

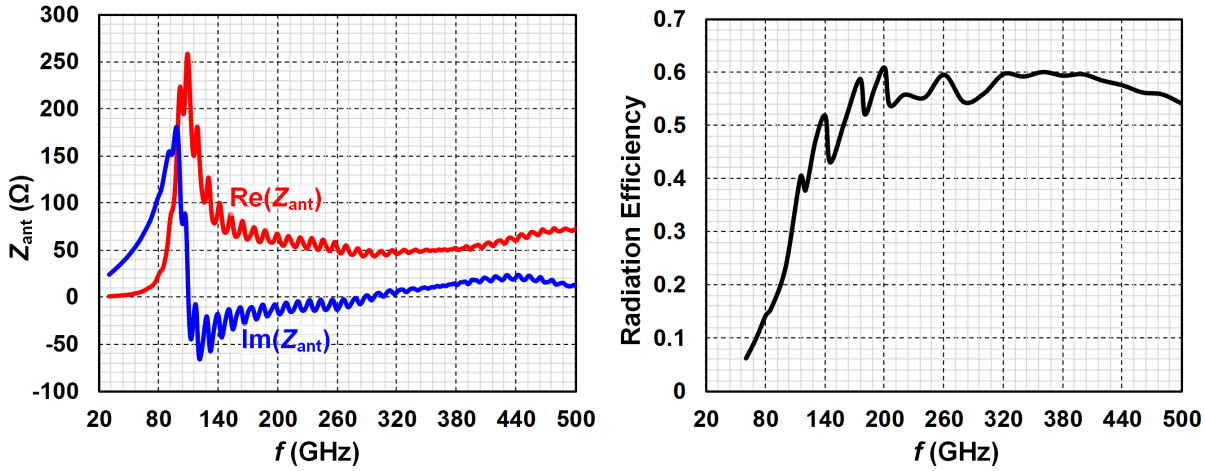

Fig. 4. Antenna impedance and radiation efficiency

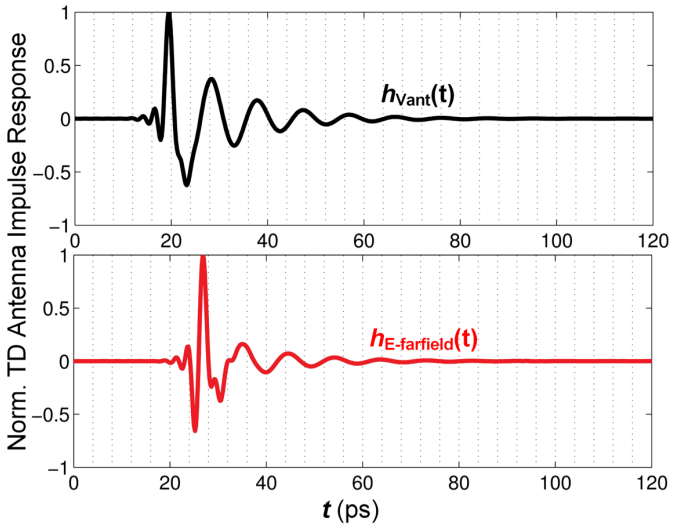

Fig. 5. Antenna induced voltage and E-farfield impulse response in time-domain

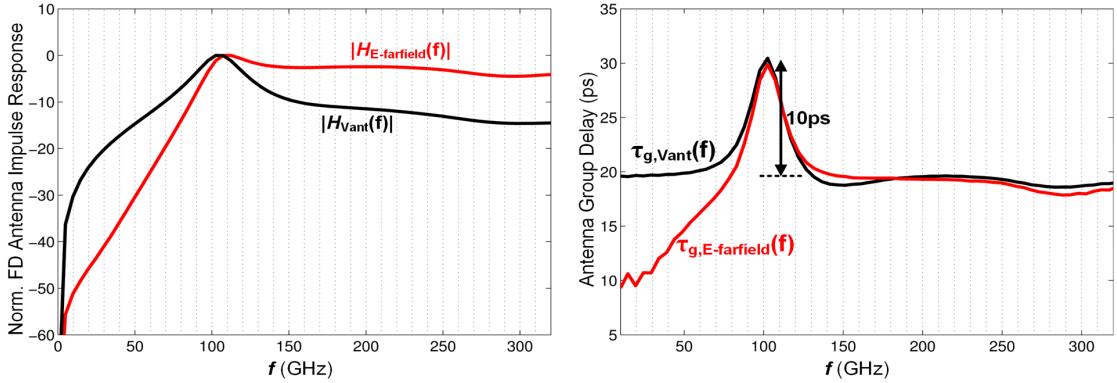

Fig. 6. Antenna induced voltage and E-farfield frequency-domain impulse response and group delay

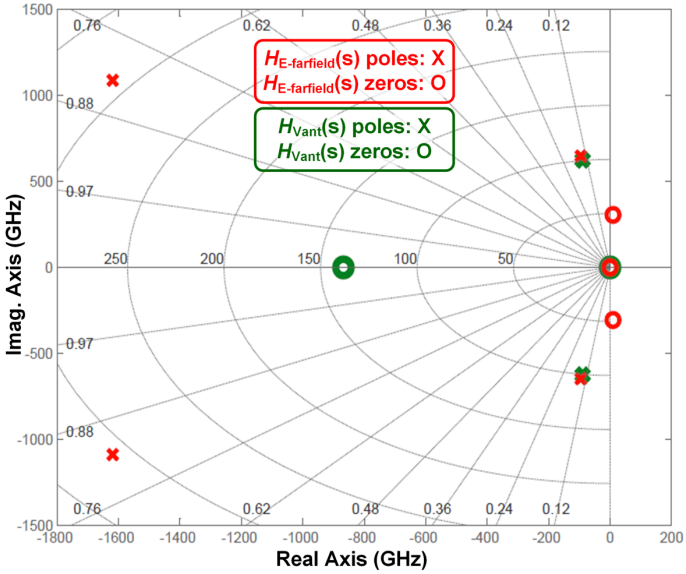

Fig. 7. Pole-zero maps of induced voltage and E-farfield transfer functions

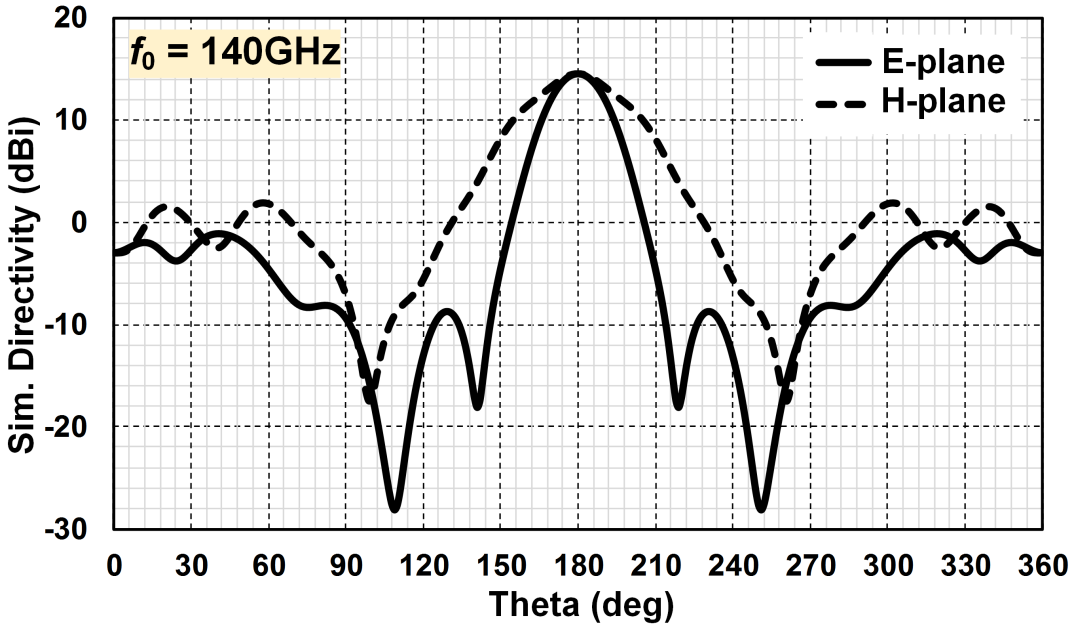

Fig. 8. Simulated E-plane and H-plane radiation pattern at 140GHz

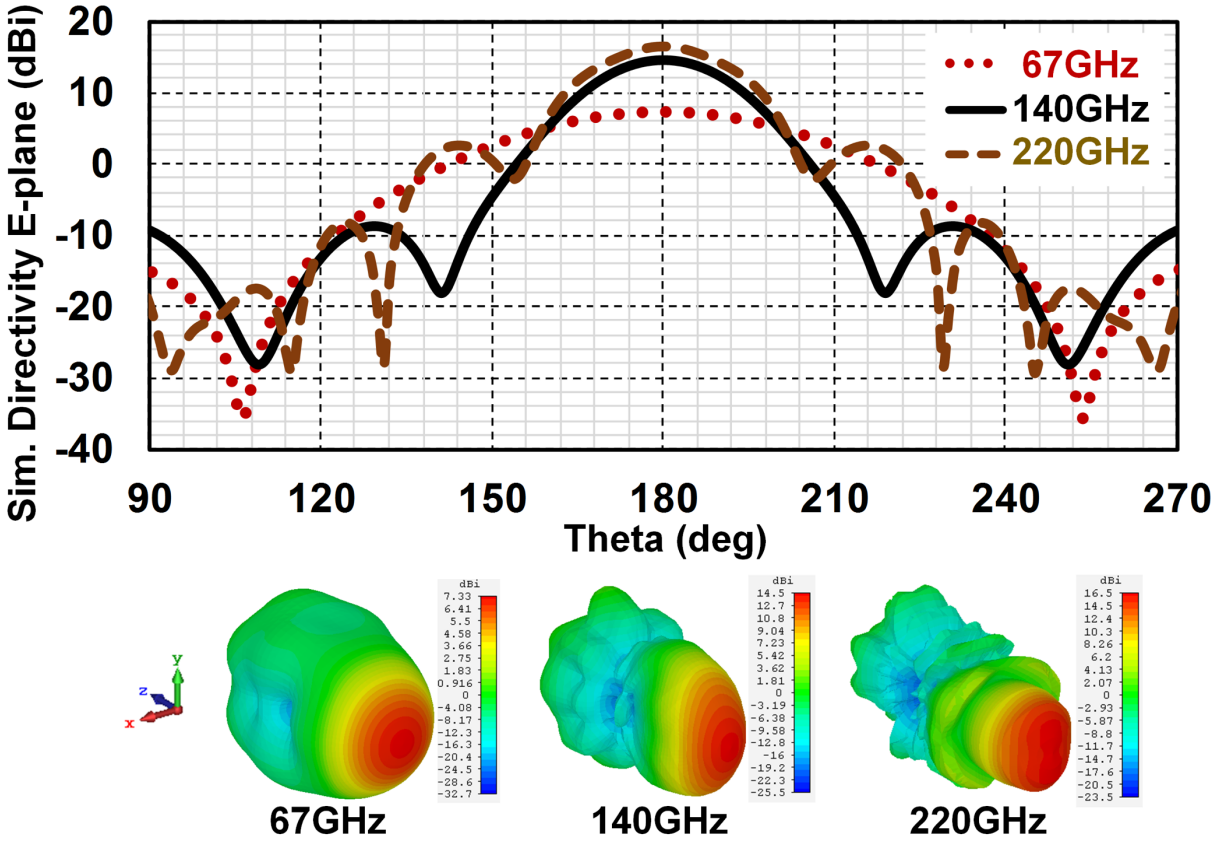

Fig. 9. Comparison of E-plane radiation pattern at f_0, $f_{-3dB,1}$, and $f_{-3dB,2}$

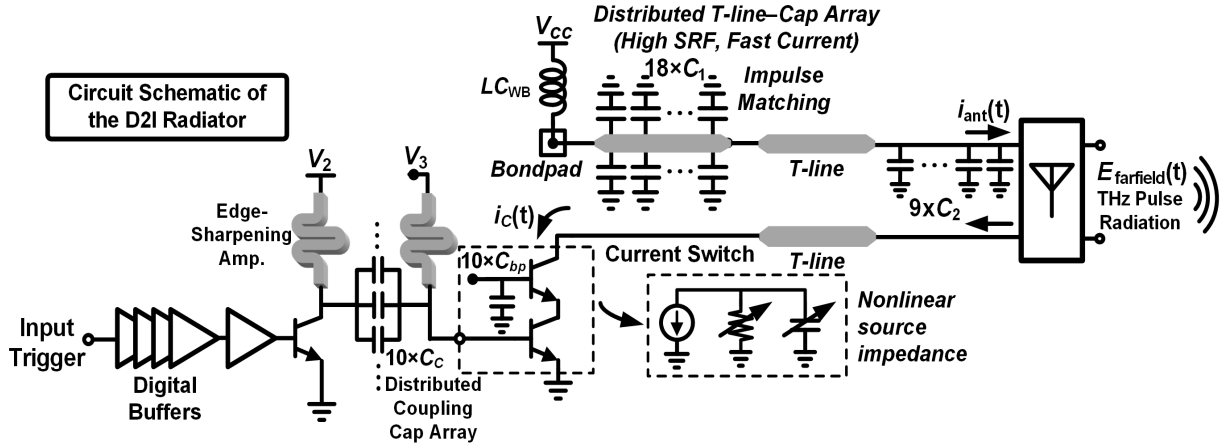

Fig. 10. Circuit schematic of D2I

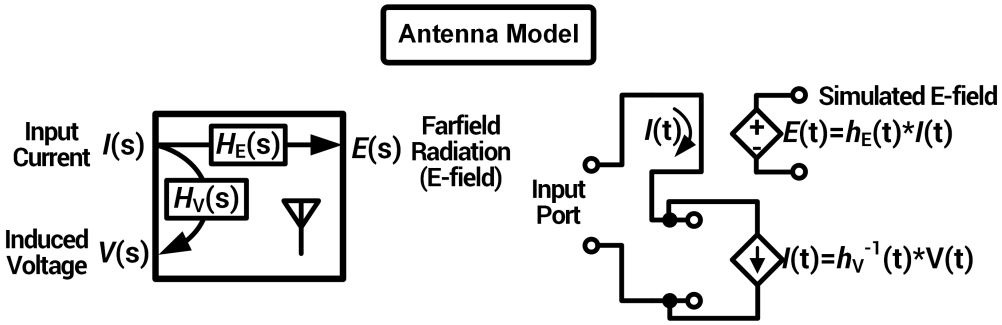

Fig. 11. Single-input, double-output antenna model for transient simulations

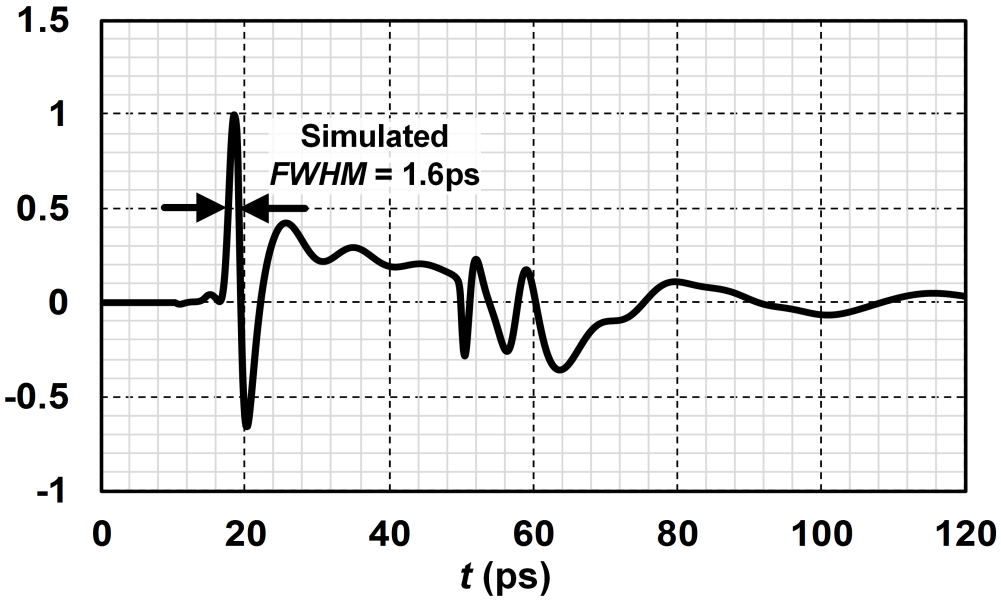

Fig. 12. Simulated radiated E-farfield

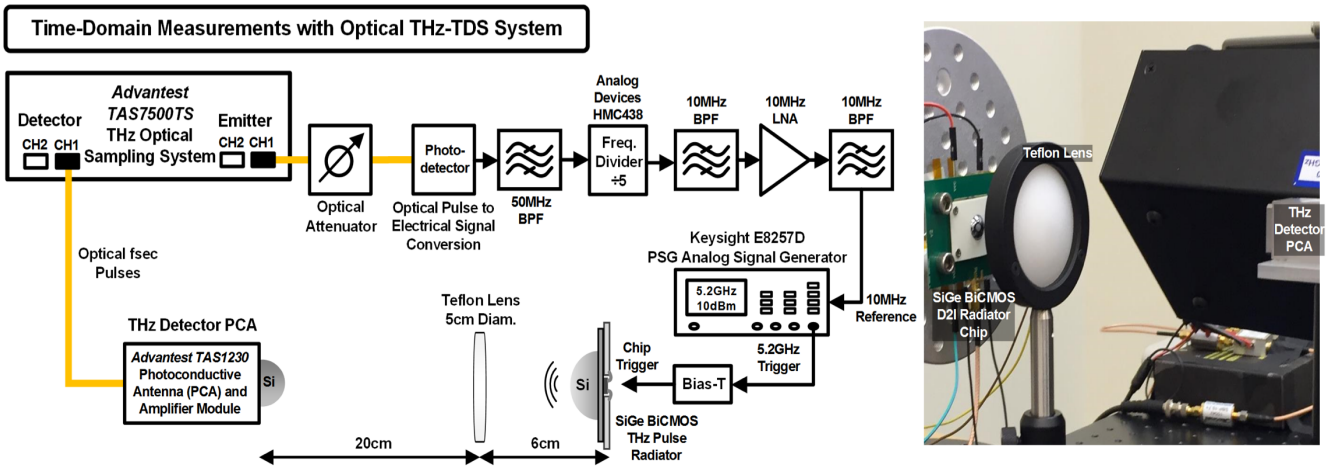

Fig. 13. Time-domain measurement setup

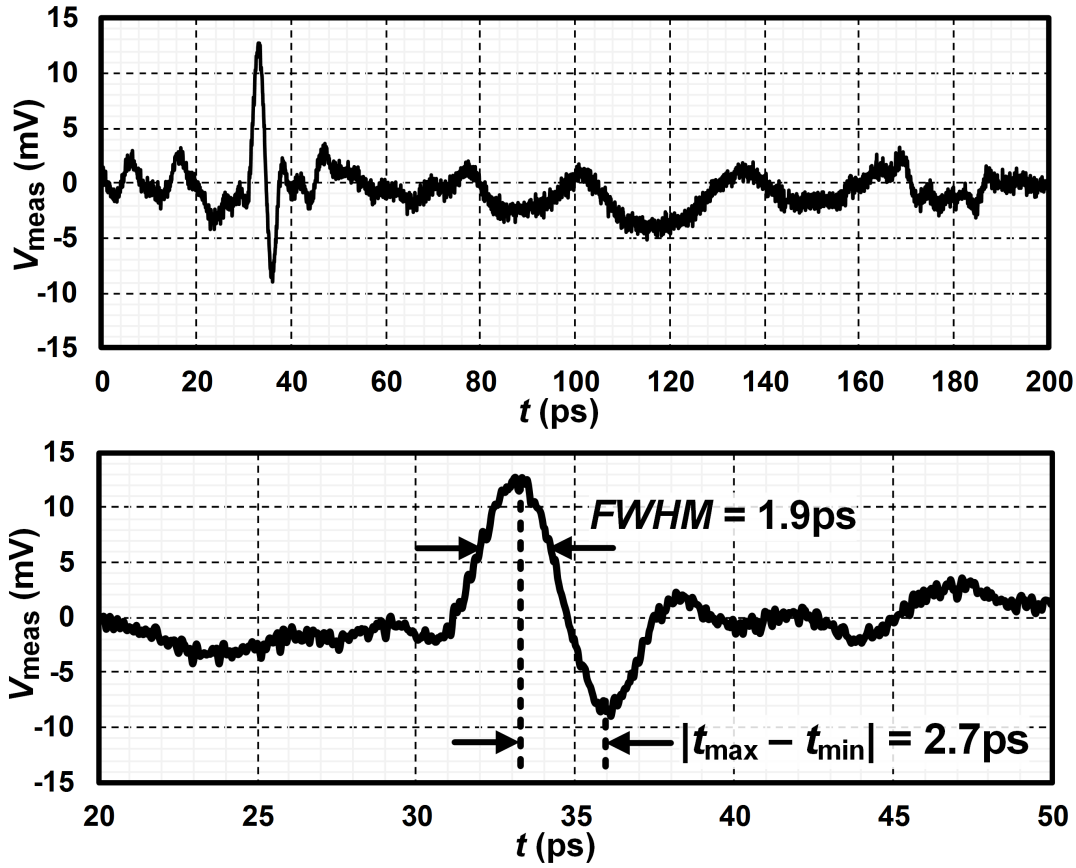

Fig. 14. THz pulse waveform measured in time-domain

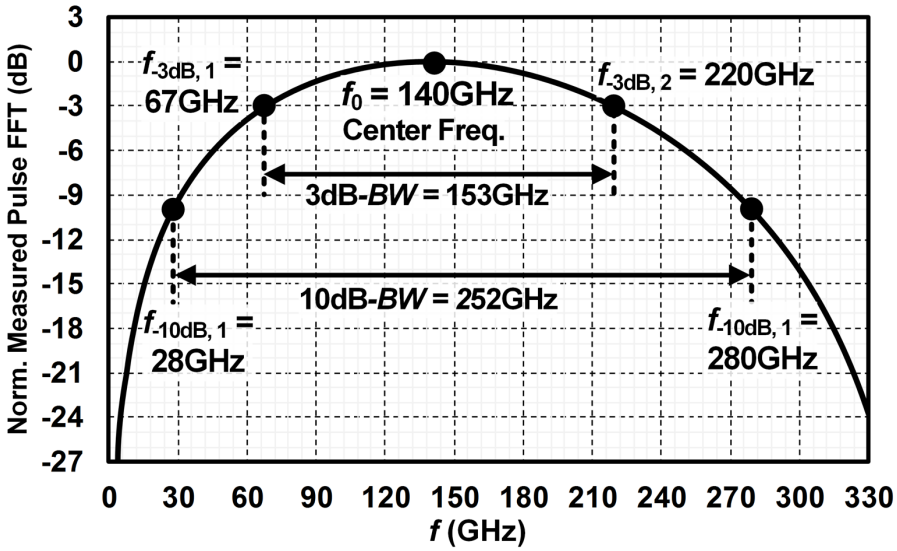

Fig. 15. Measured pulse FFT based on time-domain measurement

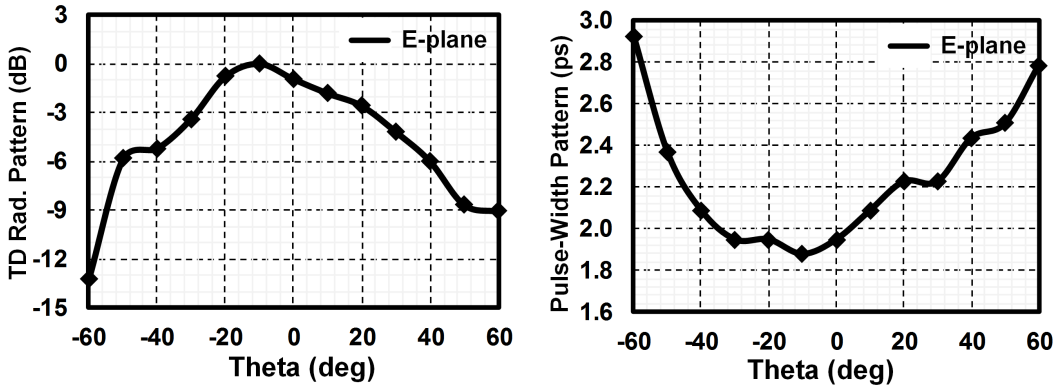

Fig. 16. Time-domain radiation patterns for peak power and pulse width (FWHM)

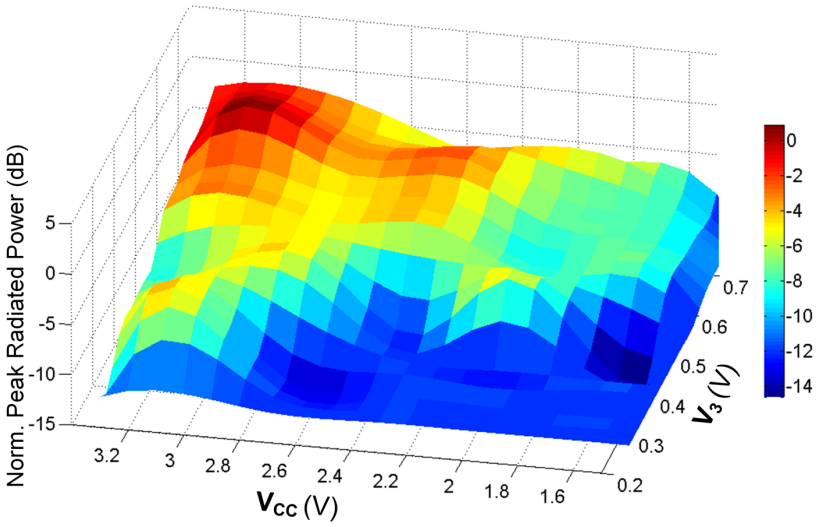

Fig. 17. Measured peak radiated power vs. current switch input biasing and supply voltage

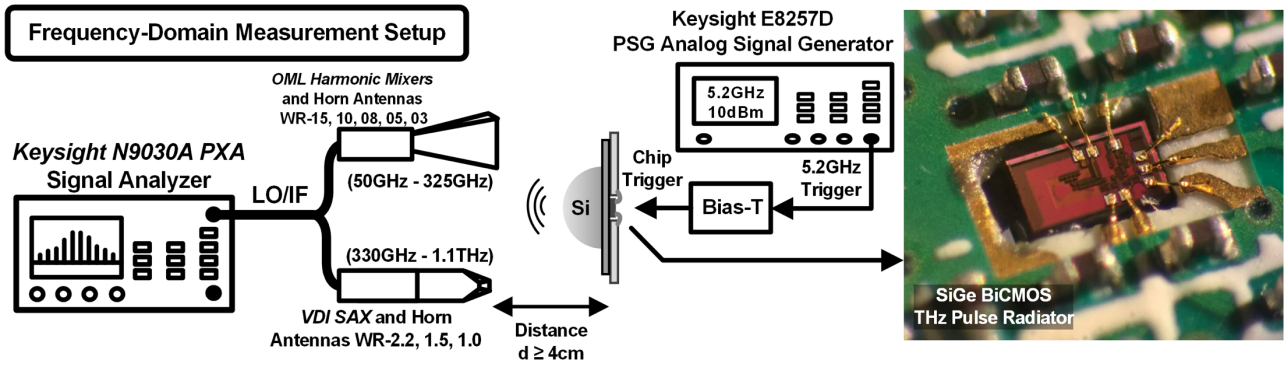

Fig. 18. Frequency-domain measurement setup

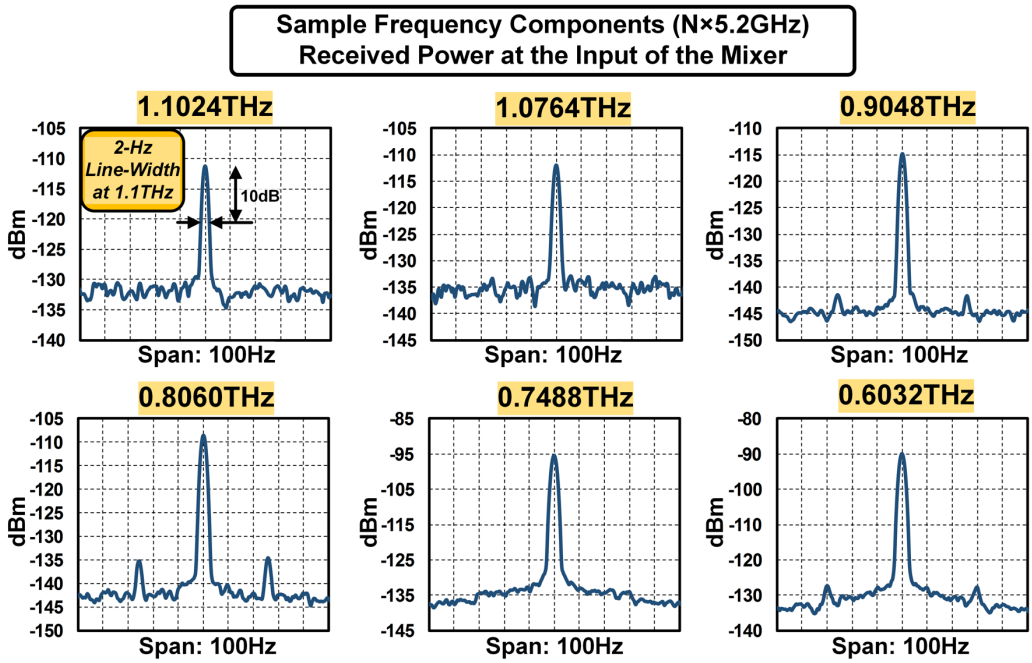

Fig. 19. Sample frequency-domain measurements of THz tones; The focus of this measurement is to show the frequency stability and the received SNR.

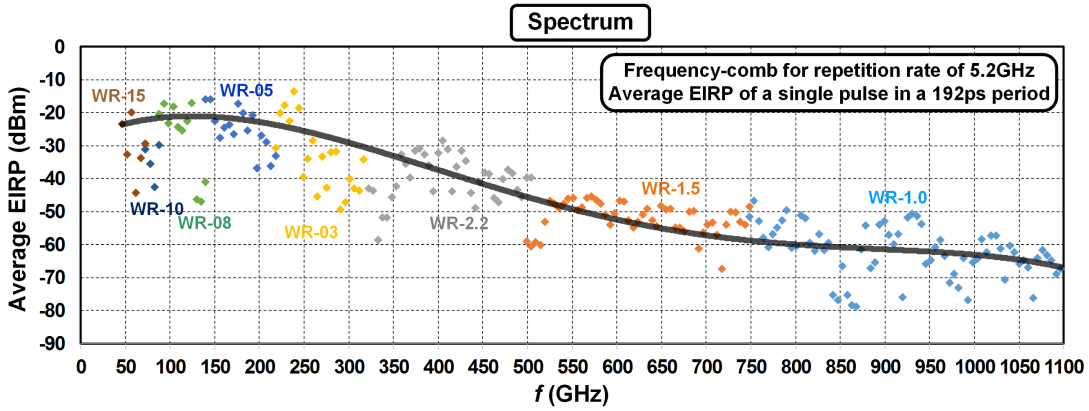

Fig. 20. Average EIRP spectrum; The fluctuations in the plot are caused by using several different mixers and antennas, and reflections from surrounding objects.

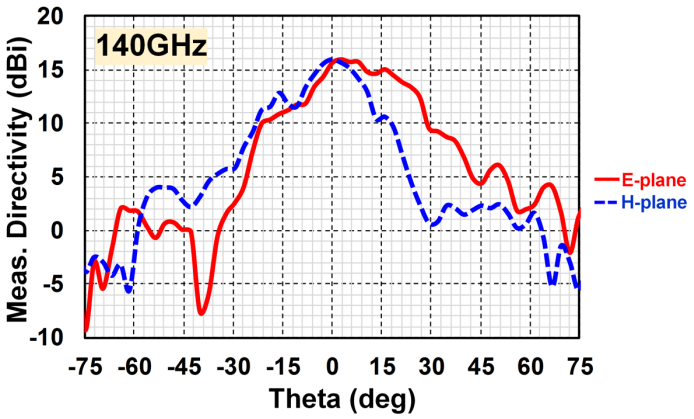

Fig. 21. Frequency-domain radiation pattern measured at the center frequency (140GHz)

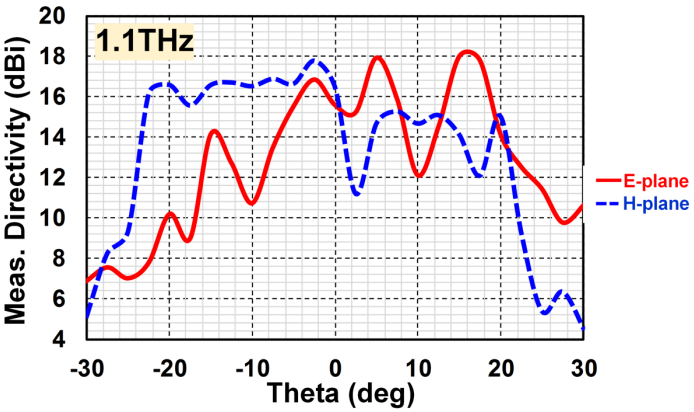

Fig. 22. Frequency-domain radiation pattern measured at 1.1THz

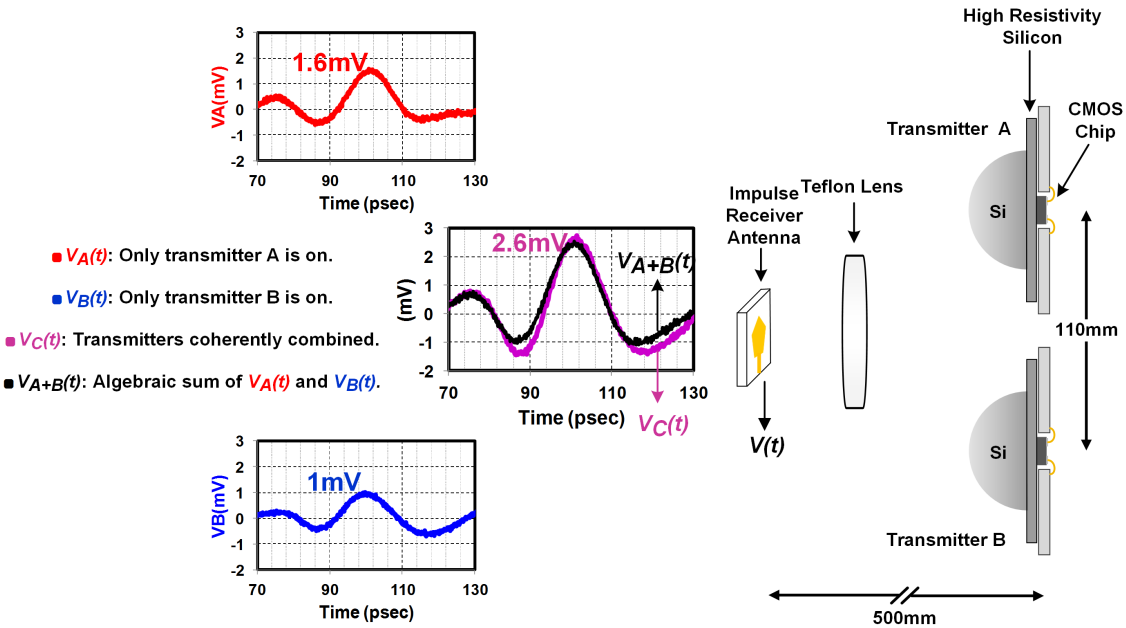

Fig. 23. Coherent spatial combining from widely spaced radiators: setup, and measurement results

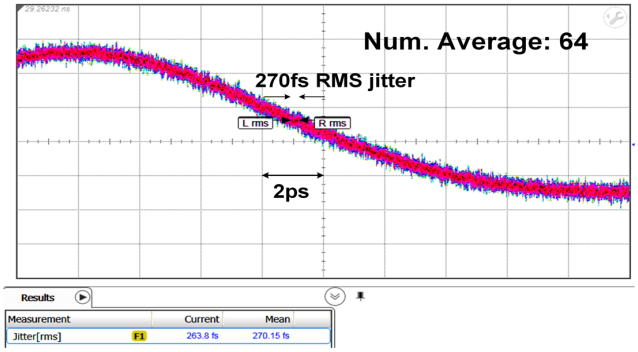

Fig. 24. Jitter of the combined signal

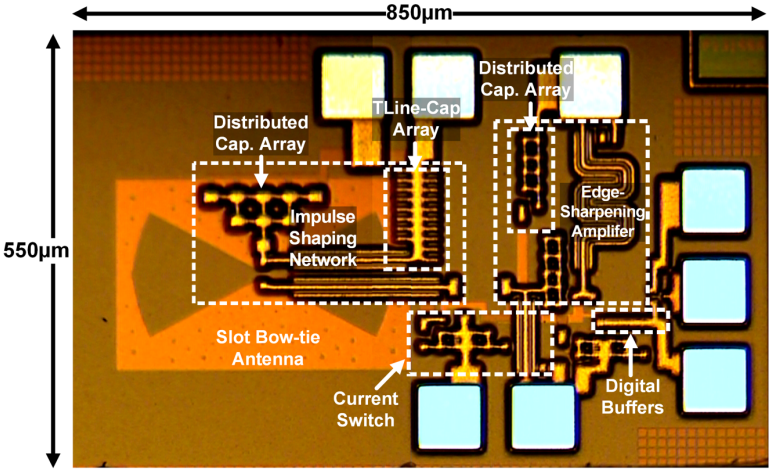

Fig. 25. Chip micrograph

Performance	This work	[5]	[6]	[7]	[17]
Highest Frequency Measured with SNR>1	1.1THz (22dB SNR)	110GHz	214GHz	N/A	N/A
Shortest Radiated Pulse Width (FWHM)	1.9ps	26ps	2.6ps*	60ps	9ps
Peak EIRP (dBm)	15	13	-3.4	15.2dBm	10
Time-Domain Measurement	Yes (with Locking)	Yes	No	Yes (with Locking)	Yes (with Locking)
Frequency-Domain Measurement	Yes (up to 1.1THz)	Yes	Yes	N/A	N/A
Coherent Spatial Combining with Multiple Chips	Performed	N/A	N/A	N/A	N/A
Pulse Generation Method	Direct Digital-to-Impulse (D2I)	Oscillator-based	Oscillator-based	Oscillator-based	Direct Digital-to-Impulse (D2I)
Power Consumption (mW)	220	580	N/A	106	260
Die Area (mm^2)	0.47 (TX)	6.16 (TX+RX)	2.5 (TX)	2.85 (TX)	0.88 (TX)
Technology	130nm SiGe BiCMOS	130nm SiGe BiCMOS	65nm CMOS	130nm SiGe BiCMOS	130nm SiGe BiCMOS

*Simulated result; not a true time-domain measurement. Only two tones used.

Table I. Comparison table